Measurements of neutron capture cross sections on ^{70}Zn at 0.96 and 1.69 MeV

L. R. M. Punte,[1] B. Lalremruata,[1,*] N. Otuka,[2] S. V. Suryanarayana,[4] Y. Iwamoto,[3] Rebecca Pachuau,[1] B. Satheesh,[1] H. H. Thanga,[1] L. S. Danu,[4] V. V. Desai,[4] L. R. Hlondo,[1] S. Kailas,[4] S. Ganesan,[5] B. K. Nayak,[4] and A. Saxena[4]

[1]*Department of Physics, Mizoram University, Tanhril-796004, Aizawl, India*

[2]*Nuclear Data Section, Division of Physical and Chemical Sciences, Department of Nuclear Science and Application, International Atomic Energy Agency, A-1400 Wien, Austria*

[3]*Japan Atomic Energy Agency, Tokai-mura, Naka-gun, Ibaraki 319-1195, Japan*

[4]*Nuclear Physics Division, BARC, Mumbai-40085, India*

[5]*Reactor Physics Design Division, BARC, Mumbai-40085, India*

(Received 24 November 2016; revised manuscript received 10 January 2017; published 28 February 2017)

The cross sections of the ^{70}Zn(n,γ) ^{71}Zn^{m} ($T_{1/2} = 3.96 \pm 0.05$-h) reaction have been measured relative to the ^{197}Au$(n,\gamma)^{198}$Au cross sections at 0.96 and 1.69 MeV using a ^{7}Li(p,n) ^{7}Be neutron source and activation technique. The cross section of this reaction has been measured for the first time in the MeV region. The new experimental cross sections have been compared with the theoretical prediction by TALYS-1.6 with various level-density models and γ-ray strength functions as well as the TENDL-2015 library. The TALYS-1.6 calculation with the generalized superfluid level-density model and Kopecky-Uhl generalized Lorentzian γ-ray strength function predicted the new experimental cross sections at both incident energies. The ^{70}Zn(n,γ) ^{71}Zn^{g+m} total capture cross sections have also been derived by applying the evaluated isomeric ratios in the TENDL-2015 library to the measured partial capture cross sections. The spectrum averaged total capture cross sections derived in the present paper agree well with the JENDL-4.0 library at 0.96 MeV, whereas it lies between the TENDL-2015 and the JENDL-4.0 libraries at 1.69 MeV.

DOI: 10.1103/PhysRevC.95.024619

I. INTRODUCTION

The neutron capture cross sections of the zinc isotopes are important both for reactor applications as well as for nuclear astrophysics. These cross sections in the energy region relevant to the *s* process were not known accurately. In order to improve the situation, Reifarth *et al.* [1] performed an experiment to study the Maxwellian averaged cross sections (MACS) of ^{64}Zn, ^{68}Zn, and ^{70}Zn neutron captures at $kT = 25$ keV, which concludes that the ^{70}Zn neutron capture MACS is about half of the value recommended by Bao *et al.* [2] although it does not have a strong impact on the *s*-process scenario. This neutron capture reaction is also a candidate of dosimetry reactions to study deviation of the epithermal reactor neutron spectrum from $1/E$ distribution [3]. Except for the thermal neutron energy, the above-mentioned $kT \sim 25$-keV spectrum averaged cross section is the unique experimental ^{70}Zn neutron capture cross section available in the EXFOR library [4], whereas comparison of evaluated cross sections in the TENDL-2015 [5], JENDL-4.0 [6,7], and EAF-2010 [8] libraries shows large discrepancies between the upper boundary of the resolved resonance region and 10 MeV. The purpose of this paper is to report new ^{70}Zn(n,γ) ^{71}Zn^{m} (3.96 ± 0.05-h) cross sections experimentally determined at incident neutron energies of 0.96 and 1.69 MeV to achieve improvement in our knowledge of this capture reaction in the fast neutron region. More details of the data analysis procedure including error analysis and numerical tables of neutron energy spectra will be published separately as an International Atomic Energy Agency (IAEA) report [INDC(IND)-0049].

*Corresponding author: marema08@gmail.com

II. EXPERIMENTAL DETAILS

A. Neutron source

The experiment was performed at the Folded Tandem Ion Accelerator (FOTIA) Facility, Nuclear Physics Division, Bhabha Atomic Research Centre (BARC), Mumbai. The protons at 2.80 and 3.50 MeV after passing through a beam collimator (0.5 cm in diameter) bombarded a 2.0-mg/cm^2-(37.4-μm)-thick natural lithium target to produce neutrons through the ^{7}Li(p,n) ^{7}Be reaction ($E_{th} = 1.881$ MeV). The proton beam energy spread is ± 0.02 MeV. A fresh lithium target was used for irradiation at each proton energy. The lithium targets were supplied by the Tata Institute of Fundamental Research (TIFR), Mumbai and prepared using the rolling method at TIFR. A 0.25-mm-thick tantalum foil (manufactured by Goodfellow Cambridge Limited, United Kingdom and supplied by H. Fillunger & Co. Pvt. Ltd., Banglore) on which the lithium target was pasted was used as a proton beam stopper. The proton beam current during irradiation varied from 50 to 100 nA, and the beam diameter on the lithium target was about 5 mm. The neutron flux was monitored online by a NE213 neutron detector at 0° and at 1-m distance from the lithium target. The neutron flux was recorded and saved every 30 min to get the neutron flux fluctuation during the whole irradiation period.

The proton beam was continuous, and therefore time-of-flight technique cannot be employed to measure the neutron flux energy spectrum. We therefore rely on the ^{7}Li(p,n) ^{7}Be neutron flux energy spectrum code EPEN [9] developed at our laboratory to obtain the neutron flux energy spectra $\varphi(E)$ for various lithium target configurations based on the ^{7}Li(p,n) ^{7}Be cross section evaluated by Liskien and Paulsen [10]. The neutron flux energy spectra $\varphi(E)$ calculated by EPEN at the two proton energies in the present experimental

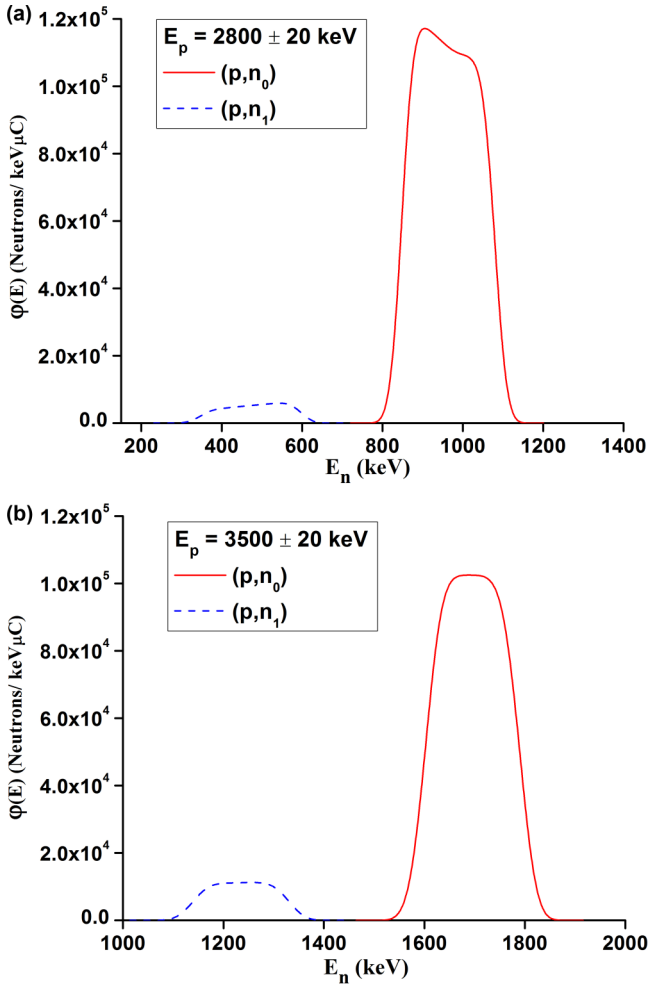

FIG. 1. Neutron flux energy spectra $\varphi(E)$ from the ^{7}Li(p,n_0) ^{7}Be and ^{7}Li(p,n_1) ^{7}Be reactions at (a) $E_p = 2800 \pm 20$ keV (b) $E_p = 3500 \pm 20$ keV obtained from the code EPEN.

configuration are shown in Figs. 1(a) and 1(b). It can be seen that the neutron energy is quasimonoenergetic due to the proton energy loss in the lithium target and due to the finite angular coverage of the neutron capture reaction target in the experimental setup. Since the proton energies in the present experiment are above the threshold energy of the ^{7}Li(p,n_1) ^{7}Be reaction (2.37 MeV), there are (p,n_1) low-energy background neutrons in addition to the (p,n_0) neutrons, and their contribution should be known for subtraction. The mean energy of the (p,n_0) neutron group was obtained by

$$\langle E_n \rangle = \int \varphi_0(E) E \, dE / \int \varphi_0(E) dE, \qquad (1)$$

with the EPEN (p,n_0) neutron flux energy spectrum $\varphi_0(E)$ and it is 0.96 and 1.69 MeV for $E_p = 2.80$ and 3.50 MeV, respectively. The width of the (p,n_0) spectrum is about ± 0.15 MeV at both proton energies.

B. Sample preparation

A zinc foil enriched ($72.4 \pm 1.0\%$) to ^{70}Zn (manufactured by FUSE "Integrated Plant Electrohimpribor," Russia and

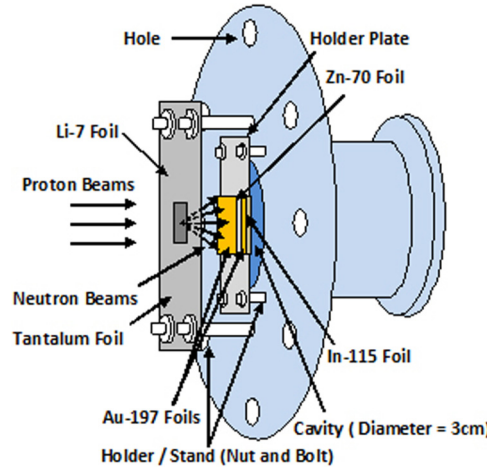

FIG. 2. The schematic of the experimental setup.

supplied by AMT Ventures Pvt. Ltd.) was sandwiched between gold foils (manufactured by Goodfellow Cambridge Limited, United Kingdom and supplied by H. Fillunger & Co. Pvt. Ltd., Banglore). The gold foils were used for normalization of the measured cross section with the ^{197}Au(n,γ) ^{198}Au standard cross section. Furthermore, another natural indium foil (provided by BARC) was stacked at the end of the foil stack to serve as an independent flux monitor foil using the ^{115}In(n,n') ^{115}In^{m} reaction for cross-checking. The whole stacked foils (10×10 mm^2) were wrapped with a 0.025-mm-thick superpure aluminum foil. The Au-Zn-Au-In stack was mounted at 0° with respect to the beam direction at a distance of 14 mm from the lithium target. All foils were weighted at TIFR with an accuracy of 0.1 mg. Details about the foils used in the experiment are given in Table I. The experimental setup is shown schematically in Fig. 2.

C. Measurement of γ-ray activity

After completion of the neutron irradiation and sufficient cooling, the foil stack was transferred to the counting room. The γ-ray activity was measured using a precalibrated lead-shielded 185-cc high-purity germanium (HPGe) detector having 30% relative efficiency and 1.8-keV energy resolution at 1.33-MeV γ energy. The data acquisition was carried out using CAMAC-based Linux Advanced Multiparameter System software (TCAMCON-95/CC 2000 crates controller and CM-48 ADCs). Therefore, the detector dead time was negligible. To correctly identify the γ ray of interest, the decay curve analysis was carried out by saving the γ count periodically as shown in Table II and followed for two to three times the half-life of ^{71}Zn^{m}. Details of decay data adopted in the analysis are given in Table III.

D. HPGe detector efficiency calibration

A ^{152}Eu point source ($T_{1/2} = 13.517$ years [14]) of known activity ($A_0 = 7582.5$ Bq on 1 Oct. 1999) was used for determination of the absolute photopeak efficiency of the HPGe detector at various characteristic γ energies of the point source. The detection efficiency for the point source placed at

TABLE I. Details of foils used in the present experiment.

Isotope	Enrichment (%)	Purity (%)	E_n (MeV)	Thickness (mg/cm^2)	Number of atoms of the isotope (10^{-4} atoms/b)
^{70}Zn	72.4 ±1.0	>99.97	0.96	87.3 ± 0.1	5.529
	8.49 (^{64}Zn)				
	8.40 (^{66}Zn)		1.69	113.6 ± 0.1	7.194
	2.01 (^{67}Zn)				
	8.70 (^{68}Zn)				
^{197}Au	100%	99.95	0.96	72.3 ± 0.1 (front)	2.211 (front)
				68.5 ± 0.1 (back)	2.094 (back)
			1.69	74.0 ± 0.1 (front)	2.263 (front)
				70.3 ± 0.1 (back)	2.149 (back)
^{115}In	95.71%	99.99	0.96	102.0 ± 0.1	5.120
			1.69	129.8 ± 0.1	6.516

a distance of 1 cm from the detector ε_p was determined by

$$\varepsilon_p = C K_c/(A_0 e^{-\lambda t} \Delta t\ I_\gamma), \quad (2)$$

where C is the number of counts during the counting time ($\Delta t = 3607$ s), A_0 is the ^{152}Eu source activity at the time of manufacture, t is the time elapsed from the date of manufacturer to the start time of counting, λ is the decay constant, I_γ is the decay γ intensity, and K_c is the correction factor for the coincidence-summing effect.

Since the count rate from the ^{70}Zn(n,γ) ^{71}Zn^{m} reaction is rather low, we needed to place the foil stack very close to the detector to obtain a high count rate. Therefore, the efficiency calibration source also had to be placed at the same distance, which is 1 cm from the detector. However, this introduces the coincidence-summing effect. Evaluations of the coincidence-summing effect and detection efficiency are discussed in the following sections. Note that all parameters independent of γ energies are finally canceled because we need only the ratio of detection efficiencies in the determination of the cross sections.

1. Coincidence summing effect

When two γ rays emitted in a cascade are detected within the resolving time of the detector, the detector cannot distinguish between the two γ rays and thus giving rise to a single signal in the spectrum as if a single γ ray would have been detected. This is known as "cascade" or "true coincidence" summing. This leads to (1) a loss in count ("summed out") from the peaks corresponding to two γ rays and (2) an addition of count ("summed in") at the sum of two energies. For any source-to-detector distance, there will be some degree of summing depending on the detector size, beyond a certain distance, coincidence-summing losses will be negligible [15].

Table IV shows the ^{152}Eu standard source characteristic γ energies and their corresponding γ intensities considered in the detector efficiency measurement. In order to correct the measured efficiency for the coincidence-summing effect, the correction factor K_c was calculated using the Monte Carlo simulation code EFFTRAN [16]. We provided the detailed specifications of the HPGe detector (e.g., dimensions and materials of the crystal, crystal hole cavity, end cap, window, mount cup, and absorber) and the ^{152}Eu γ source (e.g., dimension, material, and characteristic γ and x rays) as inputs to the simulation. The simulation therefore takes care of γ-ray–γ-ray, γ-ray–x-ray, and x-ray–x-ray coincidences. All characteristic γ lines are affected by the summed out effect whereas only those with higher energies are affected by the summed in effect as can be seen in Table IV where the γ rays with lower energies in general have larger correction factors

TABLE II. Irradiation, cooling, and counting times.

E_n (MeV)	Irradiation time (s)	Run No.	Cooling time (s) (beam stop time-counting start time)	Counting time (s)
0.96	26580.0	1	1808.0	3875.6
		2	5705.6	3636.9
		3	9373.5	7313.7
		4	16746.2	7212.3
		5	24012.5	1836.0
1.69	30300.0	1	1534.0	3591.2
		2	5180.2	3634.3
		3	8851.5	3616.9
		4	12541.4	7253.3
		5	20113.7	10368.6
		6	30573.3	7950.3
		7	38531.6	6353.3

TABLE III. Decay data adopted in the present paper taken from the ENSDF library [11–13].

Nuclide	Half-life	E_γ (keV)	I_γ (%)
^{71}Zn^{m}	3.96 ± 0.05 h	386.280	91.40 ± 2.10
^{198}Au	2.6947 ± 0.0003 d	411.802	95.62 ± 0.06
^{115}In^{m}	4.486 ± 0.004 h	336.240	45.80 ± 2.20

because the loss of their counts due to the summed out effect is not or less compensated by the summed in effect.

Only the efficiency ratio is necessary for determination of the cross sections, and therefore only the uncertainties in counting statistics and γ intensity were considered in the error propagation to the efficiencies of the ^{71}Zn^{m} and ^{198}Au characteristic γ lines.

Since the calibration of the HPGe detector was carried out with the point source while the activated foil stack has finite area (1×1 cm^2), the efficiency for the point source geometry ε_p was transferred by EFFTRAN to the efficiency for the foil stack geometry ε, which is given in Fig. 3 and Table IV.

2. *Interpolation of detection efficiency*

In order to obtain the detector efficiencies at the characteristic γ energies of the ^{71}Zn^{m} ($E_{\mathrm{Zn}} = 386.280$ keV) and ^{198}Au ($E_{\mathrm{Au}} = 411.802$ keV), the pointwise efficiencies in Table IV were interpolated through the following fitting function:

$$\varepsilon(E) = \varepsilon_0 \exp(-E/E_0) + \varepsilon_c. \tag{3}$$

The fitting parameter values are given in Table V. This curve gives the detection efficiencies of the 386.28-keV γ ray of ^{71}Zn^{m} and 411.802-keV γ ray of ^{198}Au as $\varepsilon_{\mathrm{Zn}} = 1.404\,644 \pm 0.034\,969\%$ and $\varepsilon_{\mathrm{Au}} = 1.319\,418 \pm 0.034\,688\%$, respectively. The covariance between two interpolated efficiencies $\varepsilon_{\mathrm{Zn}}$ and $\varepsilon_{\mathrm{Au}}$ are obtained following the prescription by Mannhart [17]:

$$\begin{aligned}
&\mathrm{cov}(\varepsilon_{\mathrm{Zn}},\varepsilon_{\mathrm{Au}}) \\
&\quad = \exp[-(E_{\mathrm{Zn}} + E_{\mathrm{Au}})/E_0](\Delta\varepsilon_0)^2 \\
&\qquad + \left(\varepsilon_0^2 E_{\mathrm{Zn}} E_{\mathrm{Au}}/E_0^4\right) \exp[-(E_{\mathrm{Zn}} + E_{\mathrm{Au}})/E_0](\Delta E_0)^2 \\
&\qquad + (\Delta\varepsilon_c)^2 + \varepsilon_0\left[(E_{\mathrm{Zn}} + E_{\mathrm{Au}})/E_0^2\right] \\
&\qquad \times \exp[-(E_{\mathrm{Zn}} + E_{\mathrm{Au}})/E_0]\mathrm{cov}(E_0,\varepsilon_0) \\
&\qquad + [\exp(-E_{\mathrm{Zn}}/E_0) + \exp(-E_{\mathrm{Au}}/E_0)]\mathrm{cov}(\varepsilon_0,\varepsilon_c) \\
&\qquad + \left[\left(\varepsilon_0 E_{\mathrm{Zn}}/E_0^2\right)\exp(-E_{\mathrm{Zn}}/E_0)\right. \\
&\qquad \left. + \left(\varepsilon_0 E_{\mathrm{Au}}/E_0^2\right)\exp(-E_{\mathrm{Au}}/E_0)\right]\mathrm{cov}(\varepsilon_c,E_0),
\end{aligned} \tag{4}$$

with $(\Delta\varepsilon_{\mathrm{Zn}})^2 = \mathrm{var}(\varepsilon_{\mathrm{Zn}})$ and $(\Delta\varepsilon_{\mathrm{Au}})^2 = \mathrm{var}(\varepsilon_{\mathrm{Au}})$. This is further propagated to the uncertainty in the detector efficiency ratio $\eta = \varepsilon_{\mathrm{Zn}}/\varepsilon_{\mathrm{Au}}$,

$$\begin{aligned}
(\Delta\eta/\eta)^2 &= (\Delta\varepsilon_{\mathrm{Zn}}/\varepsilon_{\mathrm{Zn}})^2 + (\Delta\varepsilon_{\mathrm{Au}}/\varepsilon_{\mathrm{Au}})^2 \\
&\quad - 2\,\mathrm{cov}(\varepsilon_{\mathrm{Zn}},\varepsilon_{\mathrm{Au}})/(\varepsilon_{\mathrm{Zn}},\varepsilon_{\mathrm{Au}}),
\end{aligned} \tag{5}$$

and we finally obtain $\eta = 1.064\,59 \pm 0.002\,74$.

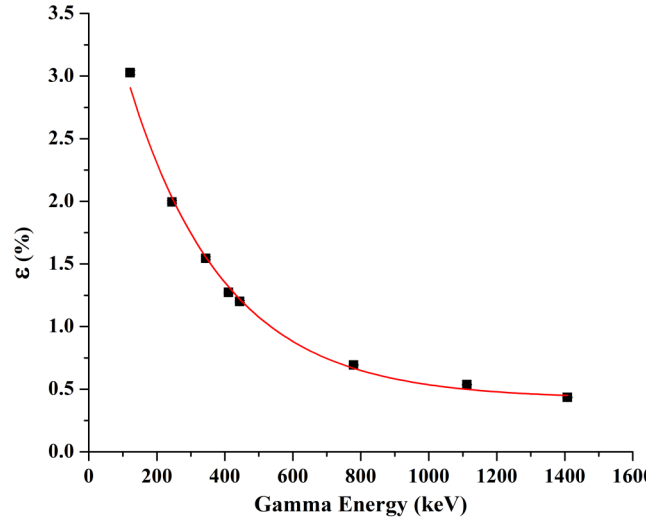

FIG. 3. Detection efficiency calibration curve of the HPGe detector for the (1×1)-cm^2 source placed at a distance of 1 cm from the detector. The error bar for the uncertainty due to counting statistics is within the symbol.

III. DATA ANALYSIS PROCEDURE

A. Estimation of the cross section and its uncertainty

The measured ^{70}Zn(n,γ) ^{71}Zn^{m} cross section $\langle\sigma^{m}_{\mathrm{Zn}}\rangle_{\mathrm{exp}}$ was derived with the ^{197}Au(n,γ) ^{198}Au reference cross section

TABLE IV. Detection efficiencies for the point source geometry ε_p and for the foil stack geometry ε at the characteristic γ energies of ^{152}Eu with their γ intensities I_γ [14] adopted for efficiency determination, counts C, and coincidence-summing effect correction factors K_c. The 444.0-keV γ line consists of 443.96 keV ($I_\gamma = 2.827 \pm 0.014\%$) and 444.01 keV ($I_\gamma = 0.298 \pm 0.011\%$) unresolved by our detector. The uncertainty in ε is propagated from the uncertainties in C and I_γ.

E_γ (keV)	I_γ(%)	C	K_c	ε_p	ε
121.8	28.53 ± 0.16	328049.3	1.113	3.0514	3.0270 ± 0.0178
244.7	7.55 ± 0.04	53997.8	1.158	2.0083	1.9940 ± 0.0136
344.3	26.59 ± 0.20	157183.5	1.078	1.5550	1.5450 ± 0.0123
411.1	2.237 ± 0.013	9647.2	1.193	1.2803	1.2720 ± 0.0149
444.0	3.125 ± 0.018	13292.1	1.142	1.2087	1.2013 ± 0.0125
778.9	12.93 ± 0.08	32542.8	1.112	0.6964	0.6922 ± 0.0058
1112.1	13.67 ± 0.08	28712.2	1.033	0.5399	0.5368 ± 0.0045
1408.0	20.87 ± 0.09	34940.8	1.050	0.4374	0.4349 ± 0.0030

TABLE V. The efficiency curve fitting parameter values.

Parameter	Value	Uncertainty	Correlation coefficient		
ε_0	3.889	0.208	1.000		
E_0 (keV)	279.541	16.880	−0.843	1.000	
ε_c	0.428	0.019	0.408	−0.687	1.000

$\langle\sigma_{\rm Au}\rangle$ by

$$\left\langle\sigma^{\rm m}_{\rm Zn}\right\rangle_{\rm exp} = \langle\sigma_{\rm Au}\rangle(A_{\rm Zn}/A_{\rm Au})[(a_{\rm Au}N_{\rm Au}I_{\rm Au}\varepsilon_{\rm Au}f_{\rm Au})/ \times (a_{\rm Zn}N_{\rm Zn}I_{\rm Zn}\varepsilon_{\rm Zn}f_{\rm Zn})](C_{\rm Zn}/C_{\rm Au}), \quad (6)$$

where $A_x = \Sigma_i A_{x,i}$ is the number of counts ($A_{x,i}$ is the number of counts from the ith counting), a_x is the isotopic abundance of the sample, N_x is the number of atoms, I_x is the γ intensity, ε_x is the detection efficiency,

$$f_x = [1-\exp(-\lambda_x t_1)]\Sigma_i \exp(-\lambda_x t_{2,i}) \times [1-\exp(-\lambda_x t_{3,i})]/\lambda_x \quad (7)$$

is the timing factor for the irradiation time t_1, cooling time for the ith counting $t_{2,i}$, measuring time for the ith counting $t_{3,i}$, λ_x is the decay constant, and C_x is the correction factor (x = Zn or Au). See Tables II and III for timing parameters and decay data, respectively. The symbol $\langle\cdots\rangle$ signifies that the cross section is averaged for the (p,n_0) neutron flux energy spectrum $\varphi_0(E)$. The fractional uncertainty in the cross section was estimated by the quadrature sum of the fractional uncertainty in $\langle\sigma_{\rm Au}\rangle, A_x, a_x, N_x, I_x, f_x, C_x$ (x = Zn and Au) as well as $\varepsilon_{\rm Au}/\varepsilon_{\rm Zn}$. The fractional uncertainty in $\Delta f_x/f_x$ was determined assuming that the uncertainty is due to the uncertainty in the half-lives of ^{71}Zn$^{\rm m}$ and ^{198}Au. See the Appendix for the determination of $\Delta f_x/f_x$.

B. Reference cross section

The reference cross section $\langle\sigma_{\rm Au}\rangle$ was obtained by folding the IAEA Neutron Cross-Section Standards $\sigma_{\rm Au}(E)$ [18] with the neutron flux energy spectrum $\varphi_0(E)$ obtained by EPEN,

$$\langle\sigma_{\rm Au}\rangle = \int \varphi_0(E)\sigma_{\rm Au}(E)dE \Big/ \int \varphi_0(E)dE. \quad (8)$$

The energy integrated neutron flux determined from the ^{198}Au activity after subtracting the contributions of (p,n_1) neutrons is $\sim 1.2\times10^6$ n cm^{-2} s^{-1} at 0.96 MeV and $\sim 1.4\times10^6$ n cm^{-2} s^{-1} at 1.69 MeV. These fluxes agree well with those determined by the measured ^{115}In$^{\rm m}$ counts and the evaluated ^{115}In(n,n') ^{115}In$^{\rm m}$ cross section in the IRDF-2002 library [19] within 5%. The uncertainty in $\langle\sigma_{\rm Au}\rangle$ due to the uncertainty in the IAEA Neutron Cross-Section Standards was obtained by

$$(\Delta\langle\sigma_{\rm Au}\rangle)^2 = \Sigma_i\left[\Phi_i^2{\rm var}(\langle\sigma_i\rangle)\right]/(\Sigma_i\Phi_i)^2 + 2\Sigma_{i>j}[\Phi_i\Phi_j{\rm cov}(\langle\sigma_i\rangle,\langle\sigma_j\rangle)]/(\Sigma_i\Phi_i)^2, \quad (9)$$

where ${\rm cov}(\langle\sigma_i\rangle,\langle\sigma_j\rangle)$ and ${\rm var}(\langle\sigma_i\rangle)$ are the covariance between the ith and the jth groupwise cross sections compiled in the IAEA Neutron Cross-Section Standards and its diagonal component ($i=j$) and $\Phi_i = \int\varphi_0(E)dE$ is the neutron flux energy spectrum integrated over the ith group of the IAEA Neutron Cross-Section Standards. The summations for i and j are taken for all energy groups between 0.675 and 1.325 MeV for $\langle E_n\rangle = 0.96$ MeV neutrons (11 groups), and between 1.325 and 2.100 MeV for $\langle E_n\rangle = 1.69$ MeV neutrons (4 groups). In order to obtain the absolute covariance for the IAEA Neutron Cross-Section Standards, the relative covariance (%^{2}) compiled in the ENDF-6 format was converted to the corresponding absolute covariance (b^2) by multiplying the unweighted groupwise cross section $\langle\sigma_i\rangle$ constructed from the pointwise cross sections in the IAEA Neutron Cross-Section Standards by ourselves. The spectrum averaged cross sections are $\langle\sigma_{\rm Au}\rangle = 82.77\pm0.86$ mb at 0.96 MeV and 64.09 ± 0.92 mb at 1.69 MeV. The fractional groupwise flux $\Phi_i/\Sigma\Phi_i$ is obtained using EPEN neutron spectra, and we adopted unweighted groupwise cross sections $\langle\sigma_i\rangle$ of the IAEA neutron cross-section standard. The correlation coefficients are obtained using the following equation:

$${\rm cor}(\langle\sigma_i\rangle,\langle\sigma_j\rangle) = {\rm cov}(\langle\sigma_i\rangle,\langle\sigma_j\rangle)/[{\rm var}(\langle\sigma_i\rangle){\rm var}(\langle\sigma_j\rangle)]^{1/2}. \quad (10)$$

Similarly the covariance between two spectrum averaged cross sections at 0.96 and 1.69 MeV is obtained by $\Sigma_{i,j}[\Phi_i\Phi_j{\rm cov}(\langle\sigma_i\rangle,\langle\sigma_j\rangle)]/(\Sigma_i\Phi_i)(\Sigma_j\Phi_j)$ where the summation for i is taken for all energy groups between 0.675 and 1.325 MeV for $\langle E_n\rangle = 0.96$ MeV neutrons whereas the summation for j is taken for all energy groups between 1.325 and 2.100 MeV for $\langle E_n\rangle = 1.69$ MeV neutrons. By using the correlation coefficients ${\rm cor}(\langle\sigma_i\rangle,\langle\sigma_j\rangle)$ given in the IAEA Neutron Cross-Section Standards [18], which also are given in Table VI, we obtain 0.059 mb^2 as the covariance of the spectrum averaged cross sections between two energies.

TABLE VI. The correlation coefficient ${\rm cor}(\langle\sigma_i\rangle,\langle\sigma_j\rangle)$ in the IAEA Neutron Cross-Section Standards between $\langle E_n\rangle = 0.96$ and $\langle E_n\rangle = 1.69$ MeV neutrons.

	$E_{\rm min}$ (MeV)	$E_{\rm max}$ (MeV)	cor $(\langle\sigma_i\rangle,\langle\sigma_j\rangle)\times100$										
$E_{\rm min}$ (MeV)			0.675	0.725	0.775	0.825	0.875	0.920	0.950	0.970	0.990	1.050	1.175
$E_{\rm max}$ (MeV)			0.725	0.775	0.825	0.875	0.920	0.950	0.970	0.990	1.050	1.175	1.325
	1.325	1.500	11.87	10.39	12.03	9.145	8.119	10.56	6.673	6.962	15.54	17.22	39.12
	1.500	1.700	14.01	12.28	14.40	11.14	10.95	10.76	4.417	8.172	18.60	14.93	22.76
	1.700	1.900	10.34	9.03	10.71	8.154	9.124	7.886	6.538	7.369	13.89	10.68	12.57
	1.900	2.100	12.09	10.5	12.47	9.483	10.09	9.439	4.228	7.915	16.07	12.78	14.88

TABLE VII. Correction factors applied to the measured cross section derivation by Eq. (6).

E_n (MeV)	0.96	1.69
$C_{\mathrm{Zn,fluc}}/C_{\mathrm{Au,fluc}}$	0.869	0.748
$C_{\mathrm{Au,low}}$	0.920 (front)	0.884 (front)
	0.921 (back)	0.884 (back)
	0.921 (mean)	0.884 (mean)
$C_{\mathrm{Zn,low}}$	0.948	0.888
$C_{\mathrm{Zn,scat}}$	0.985	0.975
$C_{\mathrm{Au,scat}}$	0.985 (front)	0.981 (front)
	0.983 (back)	0.979 (back)
	0.984 (mean)	0.980 (mean)
$C_{\mathrm{Zn,attn}}$	1.015	1.016
$C_{\mathrm{Au,attn}}$	1.019 (front)	1.020 (front)
	1.010 (back)	1.010 (back)
	1.01 (mean)	1.015 (mean)

C. Corrections

The correction factor C_x in Eq. (6) is decomposed to

$$C_x = C_{x,\mathrm{fluc}} C_{x,\mathrm{low}} C_{x,\mathrm{scat}} C_{x,\mathrm{attn}}, \tag{11}$$

(x = Zn or Au). Each term is the correction factor for

(1) neutron flux fluctuation (fluc)
(2) low-energy neutron backgrounds due to $^{7}\mathrm{Li}(p,n_1)\,^{7}\mathrm{Be}$ neutrons (low)
(3) scattered neutron background originating from elastic, inelastic, and multiple scatterings in the foil stack and the surrounding materials (scat)
(4) γ-ray self-attenuation (attn).

and summarized in Table VII. Some correction factors were determined for the two gold foils separately, and their means were applied to Eq. (6) because we did not count γ rays from the two gold foils separately.

1. Neutron flux fluctuation correction factor

The effect of the fluctuation of neutron flux due to proton current fluctuation during the irradiation was taken into consideration. Its correction factor was obtained by

$$C_{x,\mathrm{fluc}} = \langle \Phi_m \rangle [1 - \exp(-\lambda_x t_1)] / \left\{ \sum_{i=1,n} \Phi_{m,i} [1 - \exp(-\lambda_x \Delta t_1)] \exp[-\lambda_x (t_1 - i\Delta t_1)] \right\}, \tag{12}$$

where $\Phi_{m,i}$ is the neutron flux measured by the NE213 monitor detector during the ith time interval ($i = 1,n$), $\Delta t_1 = t_1/n$ (i.e., 30 min) and $\langle \Phi_m \rangle = \sum_{i=1,n} \Phi_{m,i}/n$ [20,21].

2. Low-energy background neutron correction factor

The (p,n_1) low-energy neutron background was subtracted by the correction factor,

$$C_{x,\mathrm{low}} = 1 - \int \varphi_1(E)\sigma_x(E)dE \Big/ \int \varphi(E)\sigma_x(E)dE, \tag{13}$$

where $\varphi_1(E)$ is the (p,n_1) neutron flux energy spectrum calculated by EPEN [$\varphi(E) = \varphi_0(E) + \varphi_1(E)$] and $\sigma_x(E)$ is the $^{70}\mathrm{Zn}(n,\gamma)\,^{71}\mathrm{Zn^m}$ cross section taken from the TENDL-2015 library [5] or $^{197}\mathrm{Au}(n,\gamma)\,^{198}\mathrm{Au}$ cross section taken from the IAEA Neutron Cross-Sections Standards [18].

3. Scattered neutron background correction factor

Correction factors for the scattered neutron background C_{scat} originating from elastic, inelastic, and multiple scatterings in the foil stack and surrounding materials were evaluated by PHITS Ver. 2.840 [22]. The experimental setup with all materials in and around the foil stack placed downstream of the tantalum proton beam stopper in Fig. 2 was modeled in the simulation. Neutrons were generated according to the (p,n_0) neutron flux energy spectra $\varphi_0(E)$ calculated by EPEN and in the forward direction. Productions of $^{71}\mathrm{Zn^m}$ and $^{198}\mathrm{Au}$ were calculated with the (p,n_0) neutron spectra from EPEN and evaluated cross sections of all foil stacks and surrounding materials from the ACELIBJ40 library (a library in the ACE format based on JENDL-4.0). Cross sections were calculated by counting $^{71}\mathrm{Zn^m}$ and $^{198}\mathrm{Au}$ produced by all neutrons including neutrons scattered by a foil stack or surrounding material before the production (All) and those produced by neutrons not scattered before the production (True). The uncertainties in C_{scat} are about 0.5% and 0.1% for Zn and Au foils, respectively. The weighted means of C_{scat} are adopted in determination of experimental cross sections because we cannot distinguish γ rays from front and back Au foils in our measurement.

4. γ-ray self-attenuation factors

γ spectrometric analysis requires correction for the self-attenuation effect due to the interactions of the γ rays with the foil stack. Beer-Lambert's law gives the probability to find a photon penetrating a distance x in a material (volume mass density ρ) as $\exp(-\mu_m \rho x)$ where μ_m is the mass attenuation coefficient of the γ energy and material calculated by XMUDAT Ver. 1.01 [23].

If the first foil (thickness x_1) is a homogeneous source of the γ line, and it penetrates other $n-1$ foils (thickness x_i)

TABLE VIII. The $^{70}\mathrm{Zn}(n,\gamma)\,^{71}\mathrm{Zn^m}$ cross sections measured in the present experiment $\langle \sigma^{\mathrm{m}}_{\mathrm{Zn}} \rangle_{\mathrm{exp}}$ with their total uncertainties. The ratio of the evaluated cross sections in TENDL-2015 averaged by the (p,n_0) neutron flux energy spectra $\langle \sigma^{\mathrm{m}}_{\mathrm{Zn}} \rangle_{\mathrm{TENDL}}$ to the measured cross sections are also given.

E_n (MeV)	$\langle \sigma^{\mathrm{m}}_{\mathrm{Zn}} \rangle_{\mathrm{exp}}$(mb)	Correlation coefficients		$\langle \sigma^{\mathrm{m}}_{\mathrm{Zn}} \rangle_{\mathrm{TENDL}} / \langle \sigma^{\mathrm{m}}_{\mathrm{Zn}} \rangle_{\mathrm{exp}}$
0.96 ± 0.15	1.83 ± 0.16	1.00		1.89
1.69 ± 0.15	1.33 ± 0.09	0.12	1.00	1.48

TABLE IX. The fractional (%) partial uncertainty in the measured cross sections propagated from various sources of uncertainties. The last column gives the property of the correlation between two data points for each source of the uncertainty. See the Appendix for the propagation of the uncertainties in the half-lives.

Source		$E_n = 0.96$ MeV	$E_n = 1.69$ MeV	Correlation property[a]
Count	Zn	7.809	5.988	Uncorrelated
	Au	3.247	2.471	
Sample	Zn enrichment	1.381		Fully correlated
	Zn thickness	0.115	0.088	Uncorrelated
	Au thickness	0.099	0.097	
Decay data	Zn intensity	2.298		Fully correlated
	Au intensity	0.063		
	Zn half-life	0.177	0.273	
	Au half-life	0.027	0.015	
Other	Efficiency ratio	0.257		Fully correlated
	Au standard	1.043	1.433	Partially correlated[b]
Total		8.94	7.17	Partially correlated[c]

[a]Uncorrelated, fully correlated, and partially correlated mean the correlation coefficient is 0, 1, or between them, respectively. See Ref. [35,36] for more details.
[b]Correlation coefficient is 0.07.
[c]Correlation coefficient is 0.12.

before reaching the detector, the probability of the penetration is expressed by [24–26]

$$C_{\rm attn}^{-1} = \left[(1/x_1)\int_0^{x_1} \exp(-\mu_{m,1}\rho_1 x)dx\right] \times \prod_{i=2,n} \exp(-\mu_{m,i}\rho_i x_i) = \{[1-\exp(-\mu_{m,1}\rho_1 x_1)]/(\mu_{m,1}\rho_1 x_1)\} \times \prod_{i=2,n} \exp(-\mu_{m,i}\rho_i x_i). \quad (14)$$

IV. NUCLEAR MODELS

The excitation function of the ^{70}Zn(n,γ) ^{71}Zn$^{\rm m}$ reaction from 0.4 to 2.5 MeV has been calculated using the nuclear reaction model code TALYS-1.6 [27], which was then compared with the measured cross sections. The optical model parameters for neutrons were obtained by a local potential proposed by Koning and Delaroche [28]. The compound nucleus contribution was calculated by the Hauser-Feshbach model [29]. The following five-level density models available in TALYS-1.6 [27] were used:

(1) ldmodel1: the constant temperature and Fermi-gas model where the constant temperature model is used in the low excitation region and the Fermi-gas model is used in the high excitation energy region. The transition energy is around the neutron separation energy.
(2) ldmodel2: the backshifted Fermi-gas model.
(3) ldmodel3: the generalized superfluid model.
(4) ldmodel4: the microscopic level densities from Goriely's table [30].
(5) ldmodel5: the microscopic level densities from Hilaire's combinatorial table [30].

The sensitivity of five different γ-ray strength functions available in TALYS-1.6 listed below has also been studied:

(1) strength 1: Kopecky-Uhl generalized Lorentzian [31]
(2) strength 2: Brink [32] and Axel Lorentzian [33]
(3) strength 3: Hartree-Fock BCS tables [30]
(4) strength 4: Hartree-Fock-Bogolyubov tables [30]
(5) strength 5: Goriely's hybrid model [34]

The theoretical calculations have been performed using the default parameter values except for the level-density models and γ-ray strength functions.

V. RESULTS AND DISCUSSION

The measured ^{70}Zn(n,γ) ^{71}Zn$^{\rm m}$ cross sections are given in Table VIII with their overall and partial uncertainties in Table IX. In Table VIII, the ratio of the evaluated ^{70}Zn(n,γ) ^{71}Zn$^{\rm m}$ cross sections in the TENDL-2015 library folded by the (p,n_0) neutron flux energy spectra $\langle\sigma_{\rm Zn}^{\rm m}\rangle_{\rm TENDL}$ to the measured cross sections are also given. Among the latest major libraries, JENDL-4.0 also provides an original evaluated data set for the ^{70}Zn(n,γ) ^{71}Zn$^{\rm g+m}$ cross section [6,7] but not for the ^{70}Zn(n,γ) ^{71}Zn$^{\rm m}$ cross section.

Figures 4(a)–4(e) show the comparison of the present measured spectrum averaged ^{70}Zn(n,γ) ^{71}Zn$^{\rm m}$ reaction cross sections and the cross sections for monoenergetic neutrons predicted by TALYS-1.6 with various level-density models and γ-ray strength functions. A sudden decrease in the ^{70}Zn$(n,\gamma)^{71}$Zn$^{\rm m}$ cross section around 0.9 MeV is predicted by both TALYS-1.6 and TENDL-2015. This is due to the ^{70}Zn(n,n_1) ^{70}Zn inelastic-scattering channel. Figure 4 shows that the prediction by TALYS-1.6 is very sensitive to the choice of the level-density models and the γ-ray strength functions. It can also clearly be seen that TALYS-1.6 with the generalized superfluid level model (ldmodel3) along with the Kopecky-Uhl generalized Lorentzian γ-ray strength function (strength 1) in Fig. 4(c) best matches the present measured cross sections.

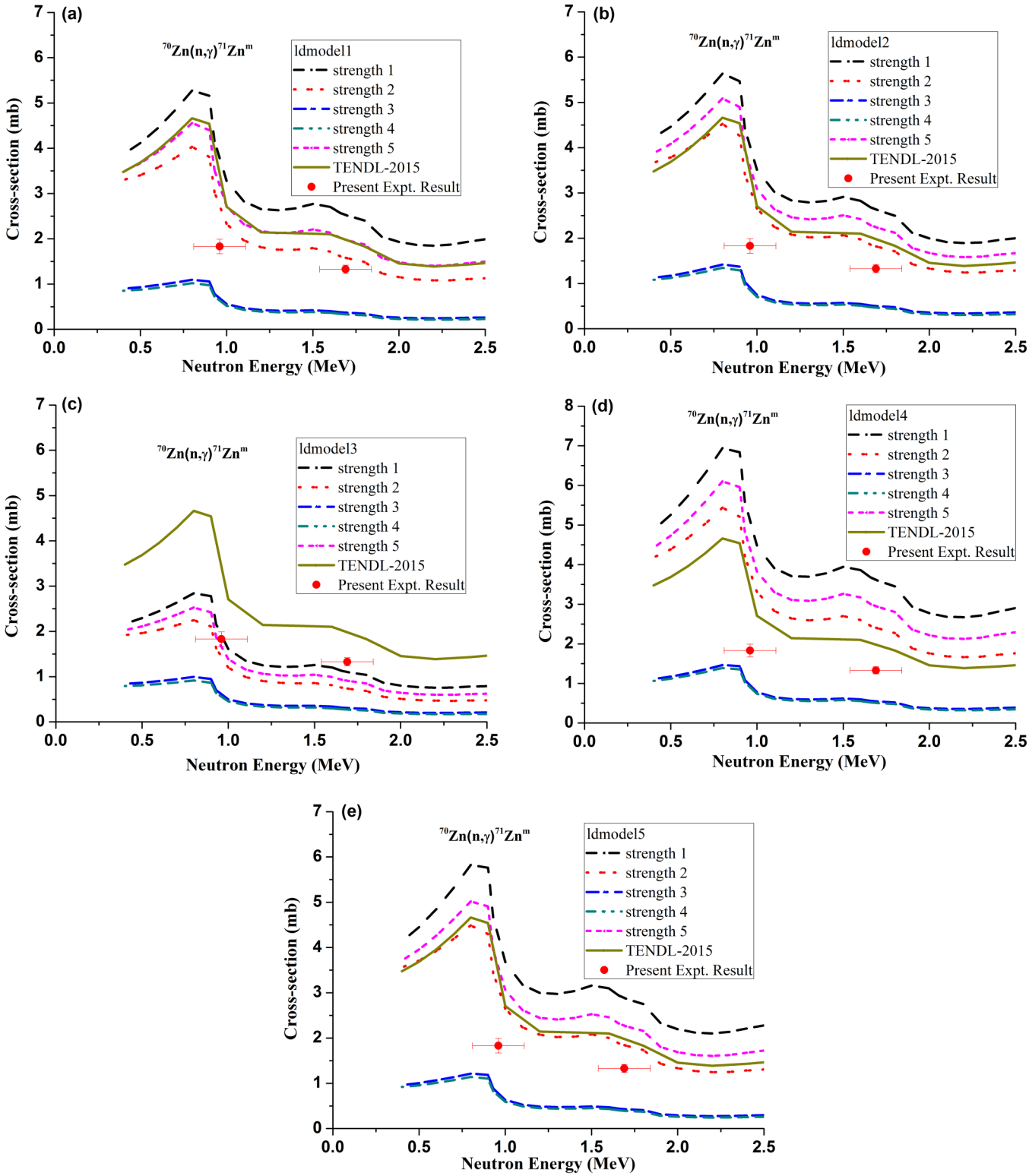

FIG. 4. Excitation functions of the ^{70}Zn(n,γ) ^{71}Zn^{m} cross sections measured in this paper, evaluated in TENDL-2015 (solid line) as well as calculated by TALYS-1.6 with five different γ-ray strength functions (strengths 1–5) with the level-density models: (a) ldmodel1 (b) ldmodel2, (c) ldmodel3, (d) ldmodel4, and (e) ldmodel5. See the text for the details of these γ-ray strength functions and level-density models. The experimental cross sections are (p,n_0) neutron flux energy spectrum averaged, whereas the evaluated and calculated cross sections are for monoenergetic neutrons.

TABLE X. The ^{70}Zn$(n,\gamma)^{71}$Zn^{g+m} capture cross sections derived from the experimental ^{70}Zn(n,γ) ^{71}Zn^{m} cross sections $\langle\sigma_{Zn}^{g+m}\rangle_{present}$. The ratio of the evaluated cross sections folded by the (p,n_0) neutron flux energy spectra for TENDL-2015 $\langle\sigma_{Zn}^{g+m}\rangle_{TENDL}$, JENDL-4.0 $\langle\sigma_{Zn}^{g+m}\rangle_{JENDL}$, TALYS-1.6 with generalized superfluid level-density model $\langle\sigma_{Zn}^{g+m}\rangle_{TALYS}$ to the present cross sections also are given.

E_n (MeV)	$\langle\sigma_{Zn}^{g+m}\rangle_{present}$ (mb)	$\langle\sigma_{Zn}^{g+m}\rangle_{TENDL}/\langle\sigma_{Zn}^{g+m}\rangle_{present}$	$\langle\sigma_{Zn}^{g+m}\rangle_{JENDL}/\langle\sigma_{Zn}^{g+m}\rangle_{present}$	$\langle\sigma_{Zn}^{g+m}\rangle_{TALYS}/\langle\sigma_{Zn}^{g+m}\rangle_{present}$
0.96 ± 0.15	3.05 ± 0.27	1.90	1.15	1.33
1.69 ± 0.15	2.24 ± 0.16	1.48	0.66	1.46

In order to estimate the ^{70}Zn(n,γ) ^{71}Zn^{g+m} cross sections from the measured ^{70}Zn(n,γ) ^{71}Zn^{m} cross sections, the measured cross sections $\langle\sigma_{Zn}^{m}\rangle_{exp}$ were multiplied by the isomeric ratios $\langle\sigma_{Zn}^{g+m}\rangle_{TENDL}/\langle\sigma_{Zn}^{m}\rangle_{TENDL}$ evaluated in TENDL-2015 folded by the ^{7}Li(p,n_0) neutron spectra. The ratios obtained are 1.6698 and 1.6823 at 0.96 and 1.69 MeV, respectively. Table X compares the derived total neutron capture cross sections $\langle\sigma_{Zn}^{g+m}\rangle_{present}$ with the (p,n_0) neutron flux energy spectrum averaged ^{70}Zn(n,γ) ^{71}Zn^{g+m} cross sections evaluated in TENDL-2015 $\langle\sigma_{Zn}^{g+m}\rangle_{TENDL}$, JENDL-4.0 $\langle\sigma_{Zn}^{g+m}\rangle_{JENDL}$, as well as calculated by TALYS-1.6 with the generalized superfluid level-density model (ldmodel3) and Kopecky-Uhl generalized Lorentzian γ-ray strength function (strength 1) $\langle\sigma_{Zn}^{g+m}\rangle_{TALYS}$.

Figure 5 shows the excitation function for the ^{70}Zn$(n,\gamma)^{71}$Zn^{g+m} reaction cross sections. It can be seen in this figure that the measured cross section is close to the JENDL-4.0 library at 0.96 MeV whereas it is between TENDL-2015 and JENDL-4.0 libraries at 1.69 MeV.

VI. SUMMARY AND CONCLUSION

The ^{70}Zn(n,γ) ^{71}Zn^{m} cross sections have been newly measured by a ^{7}Li(p,n) ^{7}Be neutron source at 0.96 and 1.69 MeV,

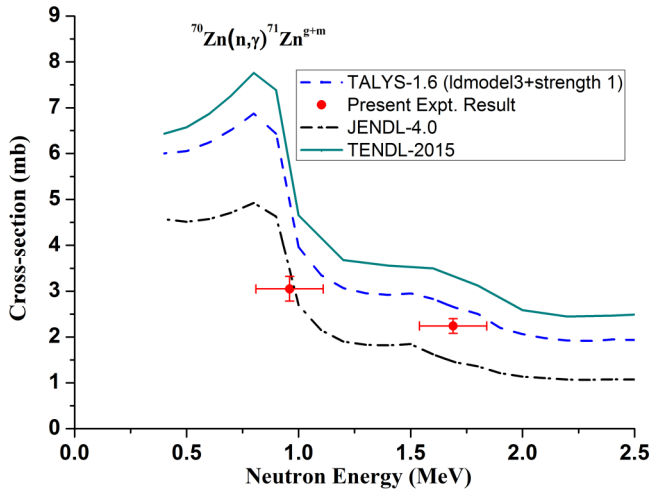

FIG. 5. Excitation functions of the ^{70}Zn$(n,\gamma)^{71}$Zn^{g+m} cross sections derived in the present paper, evaluated in TENDL-2015 and JENDL-4.0 as well as calculated by TALYS-1.6 with the generalized superfluid level-density model (ldmodel3) and the Kopecky-Uhl generalized Lorentzian γ-ray strength function (strength 1). The derived present cross sections are (p,n_0) neutron flux energy spectrum averaged, whereas the evaluated and calculated cross sections are for monoenergetic neutrons.

and their corresponding ^{70}Zn(n,γ) ^{71}Zn^{g+m} cross sections have been derived. The data analysis is carried out using the latest decay data and by taking into account the neutron flux fluctuation, low-energy (p,n_1) neutron backgrounds, scattered neutron background, and γ self-attenuation. The measured ^{70}Zn(n,γ) ^{71}Zn^{m} cross sections have been compared with theoretical calculations using TALYS-1.6 with various level-density models and γ-ray strength functions available in TALYS-1.6. It has been observed that the theoretical calculation with default parameter settings along with the generalized superfluid model (ldmodel3) and Kopecky-Uhl generalized Lorentzian γ-ray strength function (strength 1) predicts well the measured ^{70}Zn(n,γ) ^{71}Zn^{m} cross sections. The derived ^{70}Zn(n,γ) ^{71}Zn^{g+m} cross sections have also been compared with the latest evaluated cross sections in the TENDL-2015 and JENDL-4.0 libraries. It has been observed that the present derived total neutron capture cross section agrees well with the JENDL-4.0 library at 0.96 MeV whereas between TENDL-2015 and JENDL-4.0 libraries at 1.69 MeV.

ACKNOWLEDGMENTS

This work was carried out as a joint collaborative research project between the Department of Physics, Mizoram University and BARC, Mumbai under the financial support provided by the B.R.N.S., DAE, Mumbai. This work was also supported by the IAEA Nuclear Data Section. The authors are grateful to the TIFR, Mumbai for providing the lithium target. The authors also gratefully acknowledge the excellent cooperation of the FOTIA accelerator operators for the smooth operation of the machine throughout the whole experiment. Dr. Valentina Semkova (IAEA Nuclear Data Section) provided us with valuable comments on coincidence-summing effects, and they are appreciated. One of us (N.O.) expresses his special thanks for the guidance on error propagation provided by Dr. Donald L. Smith and Dr. Wolf Mannhart.

APPENDIX: DETERMINATION OF THE UNCERTAINTY IN THE TIMING FACTOR $\Delta f_x/f_x$

For the timing factor in Eq. (7),

$$f_x = [1-\exp(-\lambda_x t_1)]\Sigma_i \exp(-\lambda_x t_{2,i})[1-\exp(-\lambda_x t_{3,i})]/\lambda_x = \Sigma_i f_{x,i}, \quad \text{(A1)}$$

the uncertainty in the timing factor is

$$\begin{aligned}\Delta f_{x,i} &= (\partial f_{x,i}/\partial\lambda_x)\Delta\lambda_x \\ &= (\partial f_{x,i}/\partial\lambda_x)(d\lambda_x/dT_{1/2,x})\Delta T_{1/2,x} \\ &= (\lambda_x/T_{1/2,x})(\partial f_{x,i}/\partial\lambda_x)\Delta T_{1/2,x}, \quad \text{(A2)}\end{aligned}$$

assuming that only the uncertainty in the half-life is responsible to the uncertainty in the timing factor. The partial derivative $\partial f_{x,i}/\partial\lambda_x$ can be calculated by

$$\begin{aligned}\partial f_{x,i}/\partial\lambda_x = {} & f_{x,i}t_1\exp(-\lambda_x t_1)/[1-\exp(-\lambda_x t_1)] - f_{x,i}t_{2,i} \\ & + f_{x,i}t_{3,i}\exp(-\lambda_x t_{3,i})/[1-\exp(-\lambda_x t_{3,i})] \\ & - f_{x,i}/\lambda_x. \end{aligned} \quad \text{(A3)}$$

Finally we obtain the fractional uncertainty in f_x by

$$\Delta f_x/f_x = [\Sigma_i(\Delta f_{x,i})^2]^{1/2}/f_x, \quad \text{(A4)}$$

which is listed in Table IX as the uncertainty in the cross section due to the uncertainty in the half-life.

[1] R. Reifarth, S. Dababneh, M. Heil, F. Käppeler, R. Plag, K. Sonnabend, and E. Uberseder, Phys. Rev. C **85**, 035802 (2012).
[2] Z. Bao, H. Beer, F. Käppeler, F. Voss, K. Wisshak, and T. Rauscher, At. Data Nucl. Data Tables **76**, 70 (2000).
[3] A. Trkov (private communication).
[4] N. Otuka, E. Dupont, V. Semkova, B. Pritychenko, A. I. Blokhin, M. Aikawa, S. Babykina, M. Bossant, G. Chen, S. Dunaeva, R. A. Forrest, T. Fukahori, N. Furutachi, S. Ganesan, Z. Ge, O. O. Gritzay, M. Herman, S. Hlavač, K. Katō, B. Lalremruata, Y. O. Lee, A. Makinaga, K. Matsumoto, M. Mikhaylyukova, G. Pikulina, V. G. Pronyaev, A. Saxena, O. Schwerer, S. P. Simakov, N. Soppera, R. Suzuki, S. Takács, X. Tao, S. Taova, F. Tárkányi, V. V. Varlamov, J. Wang, S. C. Yang, V. Zerkin, and Y. Zhuang, Nucl. Data Sheets **120**, 272 (2014).
[5] A. J. Koning, D. Rochman, J. Kopecky, J. C. Sublet, M. Fleming, E. Bauge, S. Hilaire, P. Romain, B. Morillon, H. Duarte, S. C. van der Marck, S. Pomp, H. Sjostrand, R. Forrest, H. Henriksson, O. Cabellos, S. Goriely, J. Leppanen, H. Leeb, A. Plompen, and R. Mills, TENDL-2015: TALYS-based evaluated nuclear data library https://tendl.web.psi.ch/tendl_2015/tendl2015.html.
[6] K. Shibata, O. Iwamoto, T. Nakagawa, N. Iwamoto, A. Ichihara, S. Kunieda, S. Chiba, K. Furutaka, N. Otuka, T. Ohsawa, T. Murata, H. Matsunobu, A. Zukeran, S. Kamada, and J. Katakura, J. Nucl. Sci. Technol. **48**, 1 (2011).
[7] N. Iwamoto, J. Nucl. Sci. Technol. **44**, 1131 (2007).
[8] J.-C. Sublet, L. W. Packer, J. Kopecky, R. A. Forrest, A. J. Koning, and D. A. Rochman, Culham Centre for Fusion Energy Report No. CCFE-R(1)05, 2010 (unpublished).
[9] R. Pachuau, B. Lalremruata, N. Otuka, L. R. Hlondo, L. R. M. Punte, and H. H. Thanga, Nucl. Sci. Eng. (to be published).
[10] H. Liskien and A. Paulsen, At. Data Nucl. Data Tables **15**, 57 (1975).
[11] K. Abusaleem and B. Singh, Nucl. Data Sheets **112**, 133 (2011).
[12] H. Xiaolong, Nucl. Data Sheets **110**, 2533 (2009).
[13] J. Blachot, Nucl. Data Sheets **113**, 2391 (2012).
[14] M. J. Martin, Nucl. Data Sheets **114**, 1497 (2013).
[15] R. W. Damon, M.Sc. Dissertation submitted to the University of the Western Cape, July, 2005.
[16] T. Vidmar, Nucl. Instrum. Methods Phys. Res., Sect. A **550**, 603 (2005).
[17] W. Mannhart, International Atomic Energy Agency Report No. INDC(NDS)-0588 (Rev.), 2013 (unpublished).
[18] A. D. Carlson, V. G. Pronyaev, D. L. Smith, N. M. Larson, Z. Chen, G. M. Hale, F.-J. Hambsch, E. V. Gai, S.-Y. Oh, S. A. Badikov, T. Kawano, H. M. Hofmann, H. Vonach, and S. Tagesen, Nucl. Data Sheets **110**, 3215 (2009).
[19] O. Bersillon, L. R. Greenwood, P. J. Griffin, W. Mannhart, H. J. Nolthenius, R. Paviotti-Corcuera, K. I. Zolotarev, and E. M. Zsolnay, International Atomic Energy Agency Report No. STI/DOC/010/452, 2006 (unpublished).
[20] C. Sage, V. Semkova, O. Bouland, P. Dessagne, A. Fernandez, F. Gunsing, C. Nastren, G. Noguere, H. Ottmar, A. J. M. Plompen, P. Romain, G. Rudolf, J. Somers, and F. Wastin, Phys. Rev. C **81**, 064604 (2010).
[21] A. Fessler, A. J. M. Plompen, D. L. Smith, J. W. Meadows, and Y. Ikeda, Nucl. Sci. Eng. **134**, 171 (2000).
[22] T. Sato, K. Niita, N. Matsuda, S. Hashimoto, Y. Iwamoto, S. Noda, T. Ogawa, H. Iwase, H. Nakashima, T. Fukahori, K. Okumura, T. Kai, S. Chiba, T. Furuta, and L. Sihver, J. Nucl. Sci. Technol. **50**, 913 (2013).
[23] R. Nowotny, International Atomic Energy Agency Report No. IAEA-NDS-195, 1998 (unpublished).
[24] D. W. Millsap and S. Landsberger, Appl. Radiat. Isot. **97**, 21 (2015).
[25] E. Robu and C. Giovani, Rom. Rep. Phys. **61**, 295 (2009).
[26] K. R. Jackman, Ph.D. Dissertation submitted to the University of Texas at Austin, August, 2007.
[27] A. J. Koning and D. Rochman, Nucl. Data Sheets **113**, 2841 (2012).
[28] A. J. Koning and J. P. Delaroche, Nucl. Phys. A **713**, 231 (2003).
[29] W. Hauser and H. Feshbach, Phys. Rev. **87**, 366 (1952).
[30] R. Capote, M. Herman, P. Obložinský, P. G. Young, S. Goriely, T. Belgya, A. V. Ignatyuk, A. J. Koning, S. Hilaire, V. Plujko, M. Avrigeanu, O. Bersillon, M. B. Chadwick, T. Fukahori, S. Kailas, J. Kopecky, V. M. Maslov, G. Reffo, M. Sin, E. Soukhovitskii, P. Talou, Y. L. Han, and Z. G. Ge, Nucl. Data Sheets **110**, 3107 (2009).
[31] J. Kopecky and M. Uhl, Phys. Rev. C **41**, 1941 (1990).
[32] D. M. Brink, Nucl. Phys. **4**, 215 (1957).
[33] P. Axel, Phys. Rev. **126**, 671 (1962).
[34] S. Goriely, Phys. Lett. B **436**, 10 (1998).
[35] D. L. Smith and N. Otuka, Nucl. Data Sheets **113**, 3006 (2012).
[36] N. Otuka, B. Lalremruata, M. U. Khandaker, A. R. Usman, and L. R. M. Punte, Radiation Phys. Chem. (to be published).